Voltage holding and self-discharge phenomenon in ZnO-Co$_3$O$_4$ core-shell heterostructure for binder-free symmetric supercapacitors

Rajneesh Kumar Mishra [a],[*], Gyu Jin Choi [a], Hyeon Jong Choi [a], Jay Singh [b], Fateme Sadat Mirsafi [c], Horst-Günter Rubahn [c], Yogendra Kumar Mishra [c], Seung Hee Lee [d], Jin Seog Gwag [a],[*]

[a] Department of Physics, Yeungnam University, Gyeongsan, Gyeongbuk 38541, South Korea
[b] Department of Chemistry, Institute of Science, Banaras Hindu University, Varanasi 221005, UP, India
[c] Mads Clausen Institute, NanoSYD, University of Southern Denmark, Alsion 2, 6400 Sønderborg, Denmark
[d] Information Display/Energy Laboratory, Department of Nanoconvergence Engineering and Department of Polymer Nano-Science and Technology, Jeonbuk (Chonbuk) National University, Jeonju, Jeonbuk 54896, South Korea

A B S T R A C T

We report an eco-friendly, *in-situ*, and one-step synthesis of ZnO-Co$_3$O$_4$ core-shell heterostructure (ZC-CSH) using the hydrothermal process as a transcendent nanomaterial for the supercapacitor applications. The ZC-CSH SSC showed a wide potential window (1.6 V), the excellent specific capacitance of 177.0F g^{-1} at 1.4 A g^{-1}, high energy density (39.3 W h kg^{-1}), and power density (19064.3 W kg^{-1}). Further, the ZC-CSH SSC revealed excellent stability of 92.8 % after 10,000 cycles at 12.4 A g^{-1} using galvanostatic charging-discharging. Besides, the ZC-CSH SSC unraveled the outstanding stability of 96.1 % after the 8 h Voltage holding tests (VHT) at 1.6 V + 8 h Self-discharge tests (SDT). Moreover, the ZC-CSH SSC indicated a trivial leakage current of 0.06, 0.11, 0.15, and 0.17 mA during 2, 4, 6, and 8 h VHT, respectively. The ZC-CSH SSC demonstrated a voltage drop from 1.6 V to 0.39, 0.38, 0.37, and 0.36 V after 2, 4, 6, and 8 h VHT and SDT. To understand the ZC-CSH SSC's self-discharge behavior, this work explored the insights of the self-discharge mechanisms based on two thermodynamic processes, ionic concentration gradient (diffusion-control model) and potential difference (potential-driven model). Also, according to the tight-bonding (strong interactions) and loose-bonding (weak interactions), this work envisaged electrolyte ions' interactions with electrode materials to explore the coherent insights of the self-discharge behavior of the ZC-CSH SSC. It is concluded that this approach can lead to an unwavering performance of the ZC-CSH SSC for electronic portable futuristic gadgets.

1. Introduction

Recently, due to rapidly increasing tech innovations in various fields such as space exploration, the Moon missions, the Mars missions, portable electronic gadgets, electric vehicles, and military radars, there is a need for high-performance, reliable, long life, and fast chargeable energy storage systems [1–3]. On the other hand, the depletion of fossil fuels raises severe global ecological and energy concerns. Therefore, the universal energy paradigm is swiftly bending from fossil fuels to sustainable renewable energy storage sources [4]. However, the power generation from sustainable energy sources is still lagging behind the required energy in electric vehicles and portable electronic gadgets, making it challenging to find out a reliable solution to this task.

Supercapacitors, a well-known electrochemical capacitor from the family of batteries, have triggered remarkable research interests because of their features cost-effectiveness, fast charging ability, high power density, and long cycle span [5–7]. As well, several factors influence the supercapacitors' electrochemical properties in which electrode materials choice is one of them and has significant importance. The metal oxide semiconductors have been extensively studied due to their richness in the earth's crust, inexpensive and non-toxic but desperately suffer from low energy density, electronic and ionic conductivity [8,9]. To overcome these limitations, suitable and unique heterostructures need to be developed, which can fulfill insights to boost surprisingly the electrode materials properties, such as electrical, ionic conductivities, and reduce the conduction pathways during electrochemical

investigations. Therefore, electrode materials have vital significance for the fabrication of high-performance electrochemical devices.

Zinc oxide (ZnO) has a wide bandgap (3.2–3.4 eV), high mobility (130–200 cm^2 V^{-1} s^{-1}), and the conduction band edge (−4.36 eV), which are suitable as electron transporters in various applications [10]. Moreover, ZnO is an n-type and irreducible oxide semiconductor that shows one oxidation state (+2), illustrates positive valance band position, and robust oxidizing ability [11]. The ZnO attracted vast attention due to its phase stability at high temperature (~1800 °C) and Young's modulus (~150 GPa) [12]. Additionally, ZnO has received remarkable attention due to its wide range of applications in chemical, bio-sensors, organic light-emitting diodes, water splitting, and dye-sensitized solar cells [12–17]. As a result, ZnO is emerging as outstanding electrode material for electrochemical capacitor applications [18]. However, ZnO-based supercapacitors suffer from low specific capacitance and energy density, and short cycle life. The pseudocapacitance of electrochemical capacitor devices arises from faradaic redox reactions on the electrode material's surface through continuous intercalation/deintercalation of electrons and ions, which results in a short life cycle due to the surface destruction [19]. Therefore, exclusive and practical approaches have been instituted to increase the electrochemical performance of supercapacitors, included doping of different metals, heteroatom doping, morphological engineering such as hierarchical, core-shell, nanocomposites, which could make them desirable candidates for electrode materials. Besides, the Co_3O_4 nanostructure is a premium nanomaterial due to its prominent theoretical capacitance of 3560F g^{-1}, eco-friendly, p-type optical bandgap, and excellent electrochemical behaviour [19]. However, the experimental specific capacitance of Co_3O_4 does not become comparable to its theoretical capacity due to its slow electrical conduction and short-term stability during galvanostatic charging-discharging [20]. Therefore, the combination of these two nanomaterials ZnO and Co_3O_4 can be useful to improve the energy density and stability of supercapacitors, due to their excellent properties and vast applications. Significantly, the *in-situ* synthesis of a hierarchical core-shell heterostructure is favorable for growing the specific surface area and generating the nano junctions between the core (ZnO) and shell (Co_3O_4) nanostructures, which can lead to cultivating the properties and performance of the electrochemical capacitors. Therefore, the *in-situ* building of a hierarchical ZnO-Co_3O_4 core-shell heterostructure can be a promising candidate to improve the supercapacitor's overall electrochemical performance.

Recently, tremendous attention has been made to the ZnO-Co_3O_4 core-shell heterostructure for supercapacitor applications. Shaheen et al. demonstrated ZnO-Co_3O_4 nanocomposite for supercapacitor applications [18]. The supercapacitor demonstrated a power density (7.5 kW kg^{-1}), energy density (4.1 W h kg^{-1}), and specific capacitance (165F g^{-1}). Gao et al. studied the ZnO-coated Co_3O_4 nanorod-based asymmetric supercapacitor for energy storage applications [21]. The ZnO-coated Co_3O_4 nanorod-based supercapacitor exhibited high power density (7500 W kg^{-1}), energy density (47.7 W h kg^{-1}), and specific capacitance (1135F g^{-1} at 1 A g^{-1}). Furthermore, it clarified the long life of 83% after 5000 charging-discharging cycles at 10 A g^{-1}. Cai et al. studied the ZnO@Co_3O_4 core/shell heterostructures for electrochemical supercapacitor applications [22]. It was observed that the prepared electrode reveals high specific capacitance (857.7F g^{-1} at 1 A g^{-1}). It was also investigated that the ZnO@Co_3O_4 core/shell heterostructure retains its high specific capacitance (830F g^{-1}) even after 6000 cycles using charging-discharging at 6 A g^{-1}. Zhu et al. discussed the metal azolate framework-derived ZnO/Co_3O_4 for electrode materials [23]. The ZnO/Co_3O_4 electrode demonstrated high power density (1.8 kW kg^{-1}), energy density (24.3 W h kg^{-1}), and specific capacitance (830.2F g^{-1} at 1 A g^{-1}), and excellent durability (89 % after 1000 cycles using charging-discharging at 1 A g^{-1}). Hu et al. studied the ZnO/Co_3O_4 Nanobundle arrays (NBs), and Stereotaxically constricted graphene (SCG) nanomaterials based on two-terminal configurations of Asymmetric supercapacitor (ASC) [24]. The ZnO/Co_3O_4 NBs-1//SCG-ASC depicted

the high power density of 18820 W kg^{-1}, the specific capacitance of 198F g^{-1}, the energy density of 70.4 W h kg^{-1}, and admirable durability (86.5 %) after 5000 cycles using charging-discharging.

However, the lack of study on several other significant and urgent issues [like stability using voltage holding tests (VHTs), Leakage current (LC), and Self-discharge test (SDT)] in the above-discussed supercapacitors is necessary to examine. Because, these parameters have not received much attention in the rapidly increasing literature on supercapacitors. A considerable realm of self-discharge of a supercapacitor in a relaxation state considers unreliable, which makes it inappropriate during prolonged use for specific and essential purposes. Consequently, studying the mechanism behind the phenomenon of leakage current during VHTs and SDT of supercapacitors, and after that, how it can be inhibited, is extremely important for its commercial reliability.

This work unravels the Voltage holding tests (VHTs), leakage current, and Self-discharge test (SDT) of ZnO-Co_3O_4 core-shell heterostructures (ZC-CSH) based symmetric supercapacitor (ZC-CSH SSC). The ZC-CSH SSC illustrated a wide potential window (1.6 V), excellent power density, high energy density, specific capacitance, and impressive stability of 92.8 % after 10,000 GCD cycles and 96.1 % after 8 h VHT + 8 h SDT. The ZC-CSH SSC shows minimum leakage currents of 0.06, 0.11, 0.15, and 0.17 mA during 2, 4, 6, and 8 h VHT. The ZC-CSH SSC represented voltage drop from 1.6 V to 0.39, 0.38, 0.37, and 0.36 V after 2, 4, 6, and 8 h VHT and SDT. The self-discharge mechanism also interpreted the insights of the self-discharge mechanisms by potential driven and diffusion-controlled processes.

2. Experimental procedure

2.1. Materials synthesis

Ni foam substrate was first cleaned with $(CH_3)_2CO$, C_2H_5OH, and deionized (DI)-H_2O for 15 min each by using an ultrasonicator. In the first step, cobalt nitrate hexahydrate (4 mmol), zinc nitrate hexahydrate (2 mmol), ammonium fluoride (8 mmol) decomposed in 60 mL of DI-H_2O under magnetic stirring to prepare a homogeneous mixture. Further, 8 mmol of urea was mixed in the prepared mixture under vigorous stirring. In the second step, the prepared homogenous solution mixture was transferred into the 100 mL volume capacity of Teflon-lined stainless steel autoclave. The well-washed Ni foam was submerged in the homogenous mixture, and the sealed Teflon-lined autoclave was kept in a convection air oven at 120 °C for 5 h. When it was reached normal temperature, the Ni foam substrate ornamented with hydroxide precursor cleaned with DI- H_2O and ethanol and dehydrated in an air oven at 80 °C for 6 h. The hierarchical ZnO-Co_3O_4 core-shell heterostructure (ZC-CSH) was formed by annealing the dried Ni foam substrate ornamented with hydroxide precursor at 400 °C for 2 h in the air under a tubular furnace (15° per minute). The ZnO and Co_3O_4 nanostructure on Ni foam were synthesized in similar conditions using zinc nitrate hexahydrate and cobalt nitrate hexahydrate precursors, respectively.

2.2. Materials characterization

The surface morphology and elemental composition (color mapping) of prepared materials were studied using field emission scanning electron microscopy (FESEM, JEOL, JSM-7800F). The structural, morphological, and elemental analyses were investigated using transmission electron microscopy (TEM, JEOL JEM 2100F). The High-angle annular dark-field (HAADF) TEM and corresponding elemental color mapping were studied to investigate the distribution of Zn, Co, and O elements. The structural studies were investigated using X-ray diffraction (XRD, Smart Lab 3 kW, Rigaku). The elemental composition was further studied to verify the FESEM and TEM results using X-ray photoelectron spectroscopy (XPS, Kα, Thermo Scientific, UK).

2.3. Device fabrication and electrochemical measurements

As prepared, the ZnO, Co_3O_4 nanostructure, and ZnO-core-shell heterostructure (ZC-CSH) were employed as the working electrodes, Ag/AgCl (reference electrode), and Pt wire (counter electrode) in three-electrode configurations for electrochemical study in Na_2SO_4 electrolyte solution (3 M). For the fabrication of the two-electrode configuration, we used PVA/Na_2SO_4 as the electrolyte gel, Whatman filter paper (grade-2) as a separator and ZnO, Co_3O_4, and ZC-CSH on Ni foam as working electrodes. In addition, the ZC-CSH are used as working electrodes in the two-electrode configuration as ZnO-Co_3O_4//ZnO-Co_3O_4 (ZC-CSH SSC) device for electrochemical investigations. The electrochemical characterizations in three-electrode and two-electrode configurations were investigated using the Compact.h electrochemical workstation of IVIUM Technologies. In the three-electrode configuration, we studied Cyclic voltammetry (CV) at different scan rates (10 – 50 mV s^{-1}) and Galvanostatic charge–discharge (GCD) at different current densities (1.5 – 3.9 A g^{-1}) of the ZnO, Co_3O_4 nanostructure, and ZnO-Co_3O_4 core-shell heterostructure (ZC-CSH). The electrochemical impedance spectroscopy was investigated in the frequency range 0.1 Hz − 1 MHz. In the two-electrode (supercapacitor device) configuration, we studied CV at different scan rates (10 – 50 mV s^{-1}) and GCD at different current densities (1.4 – 28.6 A g^{-1}) of the ZnO-Co_3O_4 core-shell heterostructure based symmetric supercapacitor (ZC-CSH SSC). The stability of the ZC-CSH SSC was investigated using 10,000 GCD cycles. Furthermore, the stability of the ZC-CSH SSC was investigated using 8 h Voltage holding tests (VHTs) using 10 GCD cycles (at 12.4 A g^{-1}) + constant potential at 1.6 V for 2 h + 10 GCD cycles for four times. The leakage current was recorded during VHTs. The ZC-CSH SSC was charged at 1.6 V for 1 min, and after that, the Self-discharge test (SDT) was measured during Open-circuit potential (OCP) for 2 h, and repeated four times (8 h). The electrochemical impedance spectroscopy was investigated in the frequency range 0.1 Hz − 1 MHz.

3. Results and discussion

3.1. Morphological, elemental, and structural studies

Scheme 1 shows a schematic representation of *in-situ* growth on 3D Ni foam of the ZnO, Co_3O_4 nanostructure, and ZC-CSH. The Ni-foam image, FESEM images, and crystallographic illustrations of the ZnO, Co_3O_4 nanostructure, and ZC-CSH are shown in Scheme 1. A comprehensive synthesis process is described in the appropriate section of the experimental procedure.

FESEM image shows the uniform deposition of ZnO-Co_3O_4 core-shell heterostructure (ZC-CSH) on Ni-foam as a current collector substrate which was synthesized using the *in-situ* hydrothermal method, as revealed in Fig. 1(a). Fig. 1(b,c) illustrates the different magnification of the FESEM images of ZC-CSH deposited on the Ni foam substrate, which shows hierarchical, diffused, and inter-connected ZnO-Co_3O_4 core-shell spheres. As elucidated in Fig. 1(d–f), the high-magnified FESEM images indicate that the ZnO-Co_3O_4 core-shell spheres develop a 3D hierarchical structure with porous networks, improving the mass transportation and electrochemical active site assessability [25]. Furthermore, the hierarchical ZnO-Co_3O_4 core-shell heterostructures are connected to allow smooth electron transfer and shorten the joints pathways, as well as increase the electrochemical properties of supercapacitors. Further, Fig. 1(g and h) exhibits the ZnO-Co_3O_4 core-shell formation and homogeneous distribution of elements (Z, Co, and O). Inset in Fig. 1(g) reveals the FESEM Energy-dispersive X-ray spectroscopy (EDS) color mapping image of ZC-CSH with all elements together [from a selected area as exhibited in Fig. 1(d)]. It was perceived that the elements Zn, Co, and O are illustrated in purple, yellow, and green, demonstrating the fruitful development of the ZnO-Co_3O_4 core-shell structure. Fig. 1(g–i)
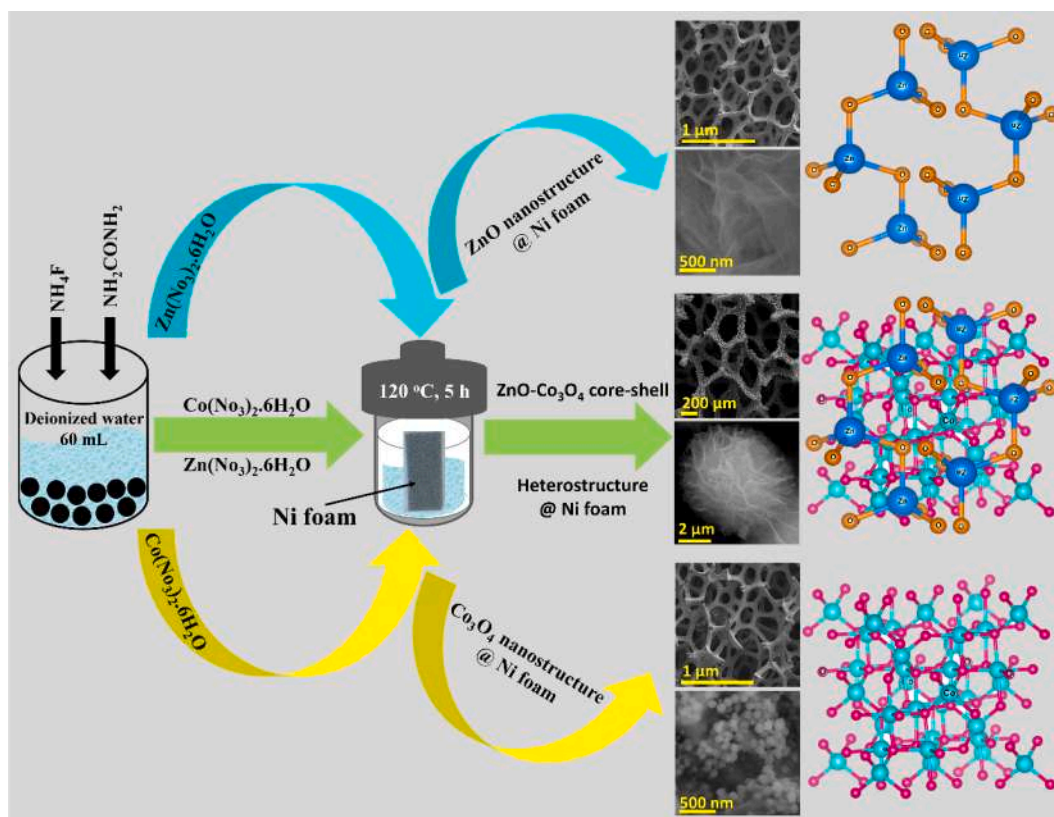
Scheme 1. (a–c) Schematic representation of synthesis process of the ZnO, Co_3O_4, and ZnO-Co_3O_4 core-shell heterostructure on 3D Ni foam. FESEM and crystallographic images of the ZnO, Co_3O_4, and ZnO-Co_3O_4 core-shell heterostructure.
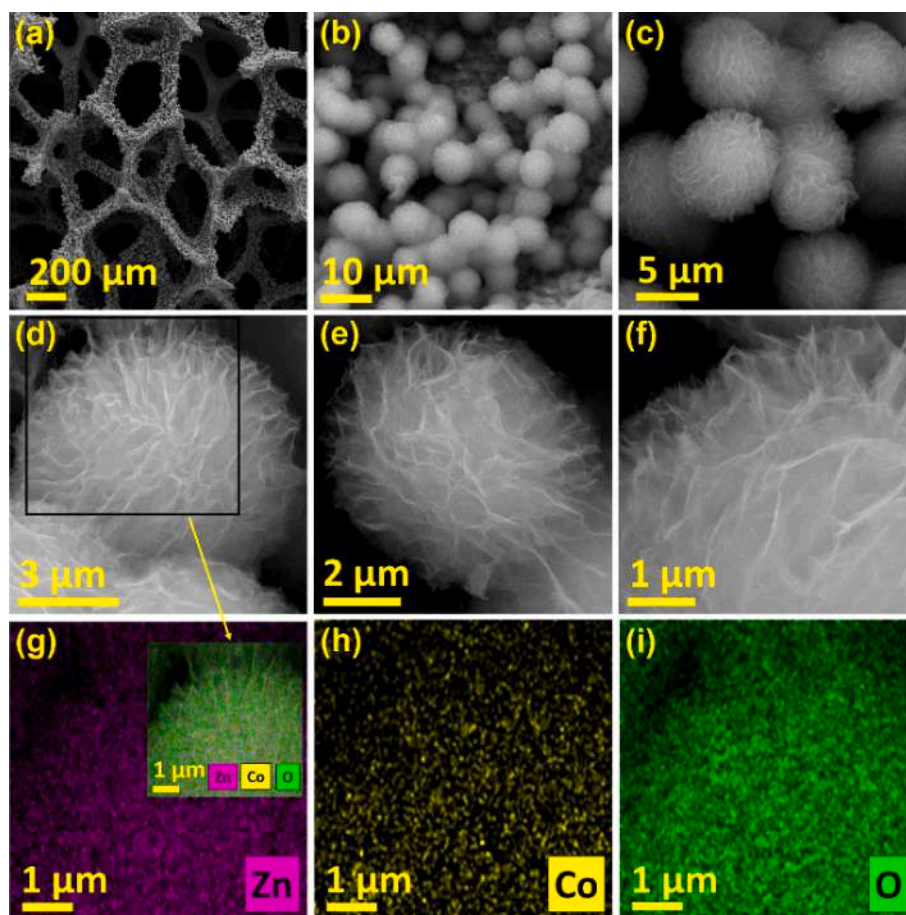
Fig. 1. FESEM images of (a) ZC-CSH in-situ grown on Ni-foam, (b-f) FESEM images of ZnO-Co$_3$O$_4$ core-shell heterostructure (inset shows the combined mapping image), and (g-i) color mapping of Zn, Co & O elements of ZC-CSH.

reveals the EDS color mapping of individual Zn, Co, and O elements, along with validating their uniform distribution in the ZnO-Co$_3$O$_4$ core-shell structure. Fig. S1(a–d) shows the FESEM images at the different magnifications of the ZnO nanostructure grown on Ni foam, implying the spherical hierarchical structures. Fig. S2(a–d) displays the FESEM images of the Co$_3$O$_4$ nanostructure grown on Ni foam at various magnifications, representing the spheres grown on the layered structure.

The ZnO, Co$_3$O$_4$, and ZnO-Co$_3$O$_4$ stabilized on Ni foam were separately ultrasonicated in ethanol to prepare the TEM samples for structural, morphological, and elemental studies. Fig. 2(a–c) demonstrates the different magnification TEM images of ZnO-Co$_3$O$_4$ core-shell heterostructure (ZC-CSH). It was recognized that the prepared ZC-CSH is highly porous and made of various small crystallites [Fig. 2(b, c)]. These porous structures were created using the annealing treatment. It is noted that porous nanostructures can enable ions' transport rate and enhance the efficient interactions between the ZC-CSH and PVA/Na$_2$SO$_4$ electrolyte-gel. Fig. 2(d) shows the HRTEM image of prepared ZC-CSH, which depicts that various sized crystallites are aggregated, overlapped, and attached. These different lattice spacing crystallites [as shown in Fig. 2(a)] correspond to the ZnO and Co$_3$O$_4$ structure of the hierarchical ZnO-Co$_3$O$_4$ core-shell heterostructure (ZC-CSH). Fig. 2(e) shows the enlarged portion of HRTEM with different lattice spacings of 0.28 nm (ZnO and Co$_3$O$_4$) and 0.47 nm (Co$_3$O$_4$) of the ZC-CSH. The observed lattice spacings and corresponding lattice planes are well-matched with JCPDS no. 36–1451 and JCPDS no. 42–1467 of the ZnO and Co$_3$O$_4$ structure, respectively [26,27]. Fig. 2(f) narrates the Fast Fourier transform (FFT) spectroscopy image of the zoomed area of the HRTEM [Fig. 2(e)] of the ZC-CSH. The FFT image shows the lattice planes (1 0 0) & (1 0 2) of the ZnO structure and the lattice planes (1 1 1) & (2 2 0) of the

Co$_3$O$_4$ structure of the ZC-CSH. Further, the HAADF TEM image and corresponding color mapping of Zn, Co, and O elements are shown in Fig. 2(g–j), which illustrates that the prepared ZC-CSH is a core-shell nanostructure. Fig. S3(a–c) shows the TEM images of the ZnO nanostructure at various resolutions. Fig. S3(d) displays the ZnO nanostructure's HRTEM image, indicating various lattice fringes of different lattice planes. Fig. S3(e,f) presents the selected zoomed area of HRTEM, and its FFT image, representing (1 0 0) and (1 0 2) lattice planes. Fig. S4 (a–c) manifests the TEM images of the Co$_3$O$_4$ nanostructure at various resolutions. It is observed that a few Co$_3$O$_4$ spheres are attached to the layered Co$_3$O$_4$ nanostructure. Fig. S4(d) displays the Co$_3$O$_4$ nanostructure's HRTEM image, indicating various lattice fringes corresponding to different lattice planes. Fig. S4(e, f) describes the zoomed area of HRTEM and its FFT image, representing (3 1 1) and (5 1 1) lattice planes corresponding to lattice spacing of 0.23 nm and 0.15 nm, respectively.

The XRD spectra of ZnO, Co$_3$O$_4$ nanostructures, and ZC-CSH is given in Fig. 3(a). The intense XRD peaks were observed at various Bragg's diffraction angles (2θ) of 31.85°, 34.49°, 36.34°, 47.67°, 56.69°, 62.96°, 68.04°, and 77.12° assigned to the lattice planes (1 0 0), (0 0 2) (1 0 1), (1 0 2), (1 1 0), (1 0 3), (1 1 2), and (0 0 4) of the ZnO nanostructure, which is well-matched with JCPDS no. 36–1451 [26]. The Bragg's diffraction peaks were observed at 31.33°, 36.91°, 44.91°, 59.46°, and 65.33°, corresponding to lattice planes (2 2 0), (3 1 1), (4 0 0), (5 1 1), and (4 4 0) of the cubic Co$_3$O$_4$ phase (JCPDS no. 42–1467) [27]. The broad Bragg's diffraction peaks (2θ) of mixed Co$_3$O$_4$ and ZnO were observed at 31.39°, 31.90°, 36.62°, 36.91°, 44.84°, 47.61°, 57.04°, 59.23°, 63.31°, 65.05°, 67.97°, and 77.19°, corresponding to the lattice planes (2 2 0), (1 0 0), (1 0 1), (3 1 1), (4 0 0), (1 0 2), (1 1 0), (5 1 1), (1 0 3), (4 4 0), (1 1 2), and
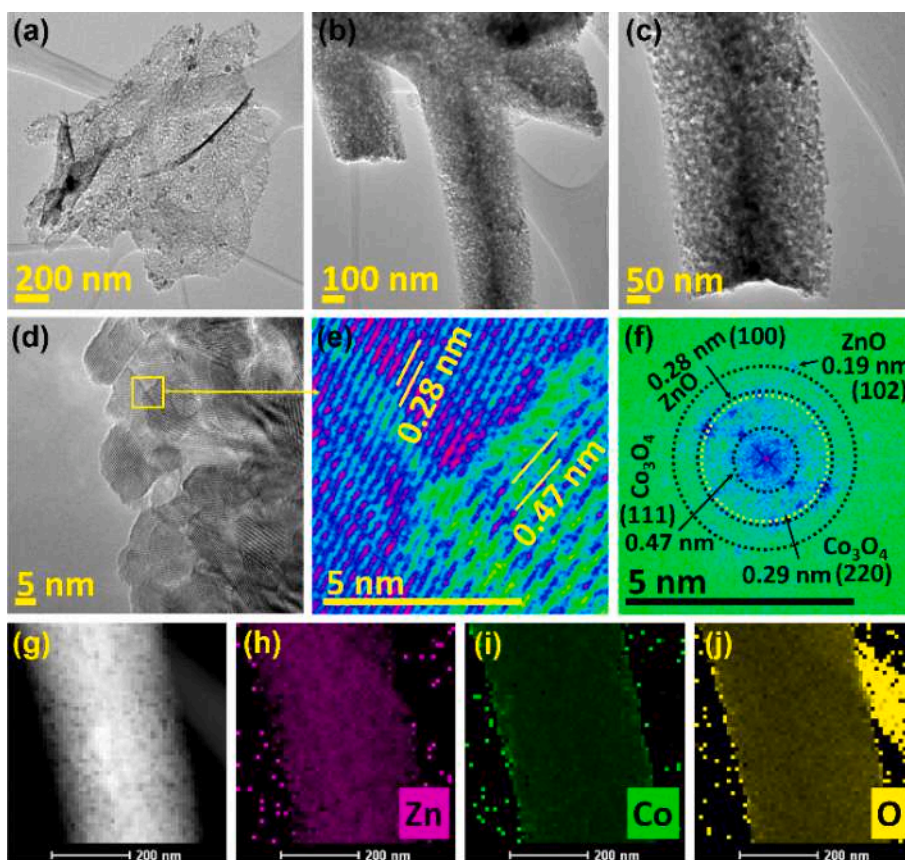
Fig. 2. (a-c) TEM images, (d) HRTEM image, (e) enlarged portion of HRTEM image, and corresponding FFT image of the ZnO-Co$_3$O$_4$ core-shell heterostructure (ZC-CSH). (g) HAADF image and corresponding color mapping of elements (h) Zn, (i) Co, and (j) O of the ZC-CSH.
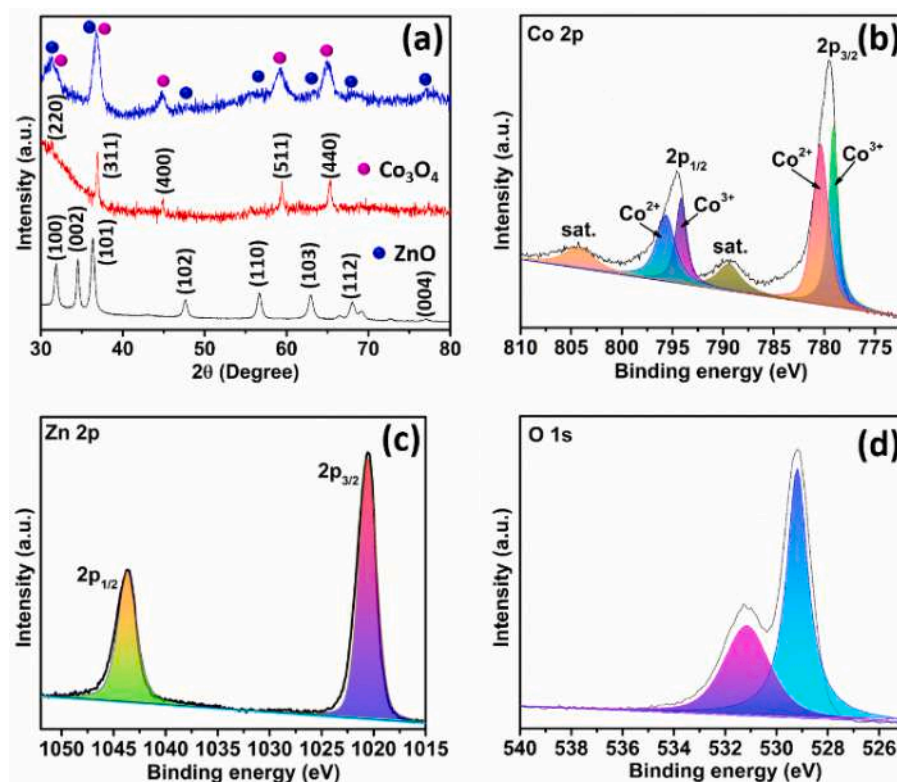
Fig. 3. (a) XRD, narrow-scan XPS spectra of (b) Co 2p, (c) Zn 2p, and (d) O 1 s of the ZnO-Co$_3$O$_4$ core-shell heterostructure.

(0 0 4), revealing the successful formation of ZnO-Co$_3$O$_4$ heterostructure. It was also noticed that the crystallite size of the ZnO-Co$_3$O$_4$ heterostructure is less compared with bare ZnO and Co$_3$O$_4$ due to broad diffraction peaks. The ZnO, Co$_3$O$_4$ nanostructures, and ZC-CSH's element's configuration and oxidation states were examined using the X-ray photoelectron spectroscopy technique. Fig. S5 shows the XPS survey spectrum of the ZnO-Co$_3$O$_4$ heterostructure, depicting characteristics peaks of Zn 2p (1019.70 eV), Co 2p (778.81 eV), and O 1 s (528.35 eV). From the high-resolution XPS spectrum of Co 2p of ZnO-Co$_3$O$_4$ heterostructure in Fig. 3(b), it can be found that there are two spin–orbit doublet peaks of Co 2p$_{3/2}$ (779.52 eV) and Co 2p$_{1/2}$ (794.49 eV) with defect (satellite) peaks at 789.40 eV and 804.21 eV. The deconvoluted spectrum of Co 2p fitted at 780.39 eV, and 795.59 eV correspond to the Co^{2+} oxidation state; however, peaks fitted at 779.05 eV and 794.09 eV are assigned to the Co^{3+} oxidation state. Fig. 3(c) displays the XPS of Zn 2p peaks of ZnO-Co$_3$O$_4$ heterostructure. The well-resolved peaks of Zn 2p peaks are observed at 1020.55 eV and 1043.67 eV, consistent with 2p$_{3/2}$ and 2p$_{1/2}$. Fig. 3(d) shows the XPS of O 1 s peak of ZnO-Co$_3$O$_4$ heterostructure. The O 1 s peak is deconvoluted into two characteristic peaks at 529.18 eV and 531.17 eV, suitable for forming lattice oxygen and metal–oxygen bonds [28,29]. Fig. S6(a) shows the survey spectrum of ZnO nanostructure, illustrating characteristics peaks of Zn 2p (1022.72 eV), and O 1 s (528.61 eV). Fig. S6(b) shows an XPS of Zn 2p peaks of the ZnO heterostructure, elucidating the 2p$_{3/2}$ (1021.45 eV) and 2p$_{1/2}$ (1044.51 eV). Fig. S6(c) displays the deconvoluted XPS spectrum of O 1 s peak of the ZnO heterostructure, elucidating the 530.29 eV and 531.83 eV. Fig. S7(a) shows the survey spectrum of Co$_3$O$_4$ nanostructure, indicating characteristics peaks of Co 2p (779.56 eV), and O 1 s (529.61 eV). The XPS of Co 2p of the Co$_3$O$_4$ nanostructure shows the two spin-orbit doublet peaks of Co 2p$_{3/2}$ (779.29 eV) and Co 2p$_{1/2}$ (794.35 eV), as shown in Fig. S7(b). The deconvoluted peaks of Co 2p fitted at 780.69 eV, and 796.16 eV correspond to the Co^{2+} oxidation state; however, peaks fitted at 779.10 eV and 794.19 eV are assigned to the Co^{3+} oxidation state. The O 1 s peak is deconvoluted into two characteristic peaks at 529.39 eV and 530.83 eV, suitable for forming lattice oxygen and metal–oxygen bonds, as characterized in Fig. S7(c).

3.2. Electrochemical study

3.2.1. Charge storage performance of electrodes in the three-electrode configuration

The 3 M Na$_2$SO$_4$ as the electrolyte, Ag/AgCl as reference electrode, Pt wire as the counter electrode, and ZnO, Co$_3$O$_4$, and ZnO-Co$_3$O$_4$ core-shell heterostructure (ZC-CSH) as working electrodes, were used in a three-electrode configuration to study the CV, GCD and specific capacitance of working electrodes. Fig. S8(a–c) shows the CV of ZnO, Co$_3$O$_4$ nanostructure, and ZC-CSH grown on Ni foam electrodes at various scan rates (10 – 50 mV s^{-1}). The CV results are shown in Fig. S8(a–c), depicting a quasi-rectangular shape that indicates the electric double-layer capacitance and pseudocapacitance behavior of electrode materials. It is also observed that the current and area under the CV curve of the ZC-CSH electrode is higher than the ZnO and Co$_3$O$_4$ nanostructured electrodes. Therefore, the ZC-CSH electrode illustrates the highest charge storage capability than the ZnO and Co$_3$O$_4$ nanostructured electrodes. Fig. S9(a–c) shows the GCD plots of ZnO, Co$_3$O$_4$ nanostructure, and ZC-CSH grown on Ni foam electrodes at the current densities of 1.5, 2.3, 3.1, 3.9 A g^{-1}. It is noticed that the quasi-triangular shape was witnessed at all current densities, illustrating the EDLC and pseudocapacitive behavior of ZnO, Co$_3$O$_4$ nanostructure, and ZC-CSH electrodes. Fig. S10 depicts the specific capacitance (evaluated using Eq. S1) of the ZnO nanostructure, Co$_3$O$_4$ nanostructure, and ZC-CSH electrodes at the various current densities. The specific capacitance values of the ZnO nanostructure electrode are 468.3, 402.7, 400.8, and 390.0F g^{-1} at different current densities. The specific capacitance values of the Co$_3$O$_4$ nanostructure electrode are 744.5, 628.0, 613.4, and 589.6F g^{-1} at different current densities. The specific capacitance values

of the ZC-CSH electrode are 1250.2, 1241.1, 1236.5, and 1229.1F g^{-1} at different current densities. The specific capacitance values of the ZnO, Co$_3$O$_4$ nanostructure, and ZC-CSH electrodes were decreased nominal at higher current densities, which is a collective feature in metal-oxide-based pseudocapacitive materials. It is also seen that the ZC-CSH electrode shows the highest specific capacitance compared with ZnO nanostructure, and Co$_3$O$_4$ nanostructured electrodes. Fig. S11 shows the EIS spectra of ZnO nanostructure, Co$_3$O$_4$ nanostructure, and ZC-CSH electrodes. The Equivalent series resistance (ESR) of the ZnO nanostructure, Co$_3$O$_4$ nanostructure, and ZC-CSH electrodes were 0.36 Ω, 0.87 Ω, and 0.05 Ω, respectively. The Charge transfer resistance (CTR) was 1.01 Ω, 1.05 Ω, and 0.45 Ω, for ZnO nanostructure, Co$_3$O$_4$ nanostructure, and ZC-CS electrodes, respectively. Therefore, EIS results illustrate that the ZC-CS electrode has the highest conduction (low ESR) than ZnO and Co$_3$O$_4$ nanostructure (high ESR). Additionally, the ZC-CS electrode shows the highest electrode material & electrolyte interaction (low CTR) than ZnO and Co$_3$O$_4$ nanostructure (high CTR).

It is concluded that the ZC-CSH electrode shows the highest electrochemical capacitive performance. Therefore, we fabricated the ZC-CSH SSC using two ZnO-Co$_3$O$_4$ core-shell heterostructure (ZC-CSH) electrodes to examine CV, GCD, specific capacitance, energy, and power density. The stability of the ZC-CSH SSC was measured using GCD cycles and voltage holding tests. Additionally, we studied the leakage current and self-discharge behavior of the ZC-CSH SSC. The self-discharge mechanism is also discussed to understand the practical energy storage devices' insights.

3.2.2. Charge storage performance of supercapacitor (two-electrode configuration)

In order to examine the current and potential of the ZC-CSH SSC, a two-electrode configuration of CV investigation was carried out. Fig. 4(a) shows the ZC-CSH SSC's CV curves, investigated at several scan rates between the voltage window of 0–1.6 V with (3 M PVA/Na$_2$SO$_4$). The CV curves maintain a quasi-rectangular shape, and current increases with scan rates which demonstrates the capacitive and reversible Faradic reactions [30]. The redox peaks in the CV curves are detected due to the concentration of H$^+$ ions in the electrolyte. H. A. Andreas et al. discussed that the concentration of the H$^+$ ions in the electrolyte is the crucial factor for the existence of the redox peaks in CV curves [31]. The non-existence or small contribution of the redox peaks in the CV curves in neutral/ alkaline solution is due to the lack of H$^+$ ions in the electrolyte. The CV curves demonstrate mainly the same shape between the scan rates of 10–50 mV s^{-1}, presenting good electrochemical capacitive characteristics of the ZnO-Co$_3$O$_4$ core–shell heterostructures [32]. For a better understanding of the charge storage mechanisms, the redox peaks were further examined to unravel the ZC-CSH SSC's kinetics processes using Dunn's method, as discussed in Fig. 4(b) [33]. The current vs. scan rates in the CV of the ZC-CSH SSC can be written in the following Eq. (1) [34].

$$i = av^b \tag{1}$$

where i, a, b, and v are the current, parameters and scan rate, respectively. When the slope (b) value is 0.5, the electrochemical reaction mechanism follows the diffusion-controlled reaction processes. If the value of b is 1, the electrochemical reaction mechanism represents capacitive processes (pseudocapacitance) due to the electrolyte ion's intercalation, or deintercalation [35]. Fig. 4(b) depicts the logarithmic plot of current density vs. scan rates using Eq. (1), which shows that the value of the slope (b) is 0.67. Therefore, it is concluded that the electrochemical reaction mechanism of the ZC-CSH SSC follows the combination of diffusion-controlled and capacitive (pseudocapacitance) reaction processes. Fig. 4(c) elucidates the Galvanostatic charging-discharging (GCD) plots of the ZC-CSH SSC at distinct current density (1.4 A g^{-1} –28.6 A g^{-1}). The GCD plots suggest the fast and reversible electrochemical characteristics of the ZC-CSH SSC. Moreover, the ZC-
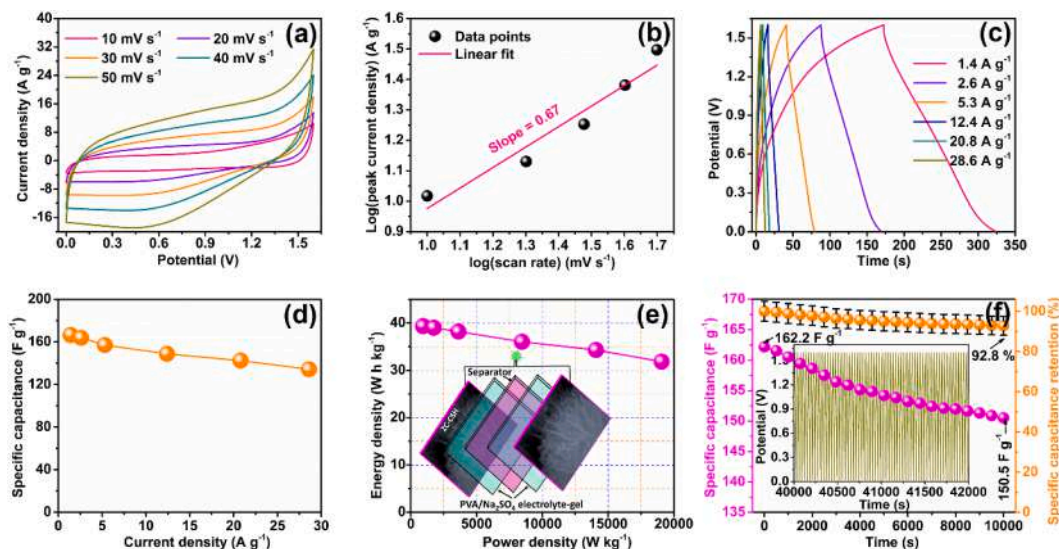
Fig. 4. (a) CV plots, (b) logarithm of the current density of cathodic peak vs. scan rates, (c) GCD plots, (d) specific capacitance vs. current density plot, (e) energy density vs. power density plot, and (f) specific capacitance and stability during 10,000 GCD cycles of ZC-CSH SSC.

CSH SSC consists of an electric double layer and pseudocapacitance behavior. Further, the ZC-CSH SSC's specific capacitances are estimated by the area under the discharge curve of GCD plots at distinct current densities using Eq. S2. The ZC-CSH SSC showed excellent specific capacitance of 177.0, 175.6, 171.8, 162.2, 154.3, and 143.3F g^{-1} at the various current density of 1.4, 2.6, 5.3, 12.4, 20.8, 28.6 A g^{-1}, respectively. It was witnessed that the specific capacitance of the ZC-CSH SSC declines with rising current density because of little ionic interaction time between electrode materials and electrolyte ions. Besides, these high specific capacitance values are mainly due to the following reasons: (i) ZnO-Co$_3$O$_4$ core-shell heterostructures pore formations provide unrestricted movement of electrolyte ions, reduce the diffusion path and decrease the diffusion resistance [36], (ii) surface capacitive effects, whether electrostatic or near-surface pseudocapacitive [37], (iii) good conductivity and chemical stability of ZnO-Co$_3$O$_4$ core-shell heterostructures, (iv) the unique morphology of ZnO-Co$_3$O$_4$ core-shell heterostructure, which enables more active surface area, more accessible active sites, and an excellent ionic/ electrical conduction during electrochemical investigations [38]. Fig. 4(e) shows the energy and power density plot (assessed by Eq. S3 and Eq. S4) of the ZC-CSH SSC. The inset in Fig. 4(e) demonstrates the schematic architecture of the ZC-CSH SSC. The calculated energy density values are 39.3, 39.0, 38.2, 36.0, 34.3, and 31.8 W h kg^{-1} at the power density values of 930.3, 1741.0, 3623.9, 8447.0, 14077.6, and 19064.3 W kg^{-1}, respectively. These energy and power density values of the ZC-CSH SSC can satisfy the energy and power consumption requirements for certain portable electronic gadget applications. Further, we have investigated the ZC-CSH SSC's working lifetime using 10,000 cycles using Galvanostatic charging-discharging (GCD) at 12.4 A g^{-1}. GCD cycling stability as an important feature is measured by the degree of wellness of the ZC-CSH SSC during its consecutively charging and discharging processes. Fig. 4(f) shows the ZC-CSH SSC's specific capacitance and stability during 10,000 GCD cycles at a current density of 12.4 A g^{-1}. The ZC-CSH SSC shows excellent stability of 92.8 % with a slight decrease (7.2 %) in its specific capacitance from 162.2F g^{-1} to 150.5F g^{-1} after 10,000 GCD cycles. The uniform distribution of the Co$_3$O$_4$ shell on the ZnO core can tune the electronic structural states, leading to resilient coupling interactions, enhancing long-term stability [39]. The outstanding stability of the ZC-CSH SSC can rely on several factors such as the synergistic effect of ZnO core and Co$_3$O$_4$ shell hierarchical heterostructure, high conductivity, no delamination or non-degradation of ZC-CSH due to its *in-situ* growth on Ni-foam, i.e., binder-free method, favorable pore structure, large

electroactive surface area, and interaction of electrolyte ions with electrode materials [40].

During the 10,000 GCD cycling test, the maximum time is dedicated to the voltages that are not important and enough for the supercapacitor's stability. Therefore, a more demanding test to investigate the supercapacitor's stability is a constant potential test at maximum device potential known as the Voltage holding tests (VHTs). Commonly, the VHTs take less time compared with the GCD cycling test before a precise outcome can be accomplished. During the voltage holding test, the maximum working voltage of 1.6 V is applied to the supercapacitor. After every four hours of the VHT (2 h) at 1.6 V and SDT (2 h), the GCD cycling was performed to evaluate the ZC-CSH SSC's specific capacitance. Fig. 5(a) shows the GCD cycles + 2 h VHT + 2 h SDT characteristics for a period of 16 h of the ZC-CSH SSC. It was noted that the ZC-CSH SSC shows excellent voltage holding and self-discharge properties after a few charging-discharging cycles. Fig. 5(b) illustrates the enlarged portion [as highlighted in Fig. 5(a)] of GCD cycles between the SDT and VHT, which are crucial for the evaluation of specific capacitance of the ZC-CSH SSC. Fig. 5(c) alludes to the GCD cycles + VHT of the ZC-CSH SSC for 8 h (the inset shows an enlarged portion of the GCD cycles before and after each 2 h VHT). This study determined the ZC-CSH SSC's durability and justified the stability results evaluated after 10,000 GCD cycles, as discussed in Fig. 4(f). By examining voltage holding tests on the ZC-CSH SSC, more information was provided on the lifetime of the energy storage systems because the VHTs allocate more time for charged species to diffuse away from the electrode surface interact with other charged species or the opposite electrode [41]. The specific capacitance and specific capacitance retention (stability) of the ZC-CSH SSC evaluated using the area under the discharge GCD cycle after 2, 4, 6, and 8 h of VHT are shown in Fig. 5(d). It was observed that the specific capacitance slowly reduces from 159.1F g^{-1} to 152.8F g^{-1} after 2 h to 8 h of VHT. It was also perceived that the stability (specific capacitance retention) of the ZC-CSH SSC is 96.1 % after 8 h of VHT, which further justified the results of stability obtained from 10,000 GCD cycles [as illustrated in Fig. 4(f)]. In addition, the reproducibility test of the ZC-CSH is also a vital parameter for its commercial use. Therefore, we fabricated three similar ZC-CSH SSCs and then studied their reproducibility using GCD cycling (12.4 A g^{-1}) + VHT. Fig. 6(a–d) elucidates the charging-discharging cycles at 12.4 A g^{-1} of three similar ZC-CSH SSCs after 2, 4, 6, and 8 h of VHT. It was noticed that the area under GCD cycles was increased for all three devices. Fig. 6(e) shows the specific capacitance of three similar ZC-CSH SSCs, calculated using Eq. S2. The specific
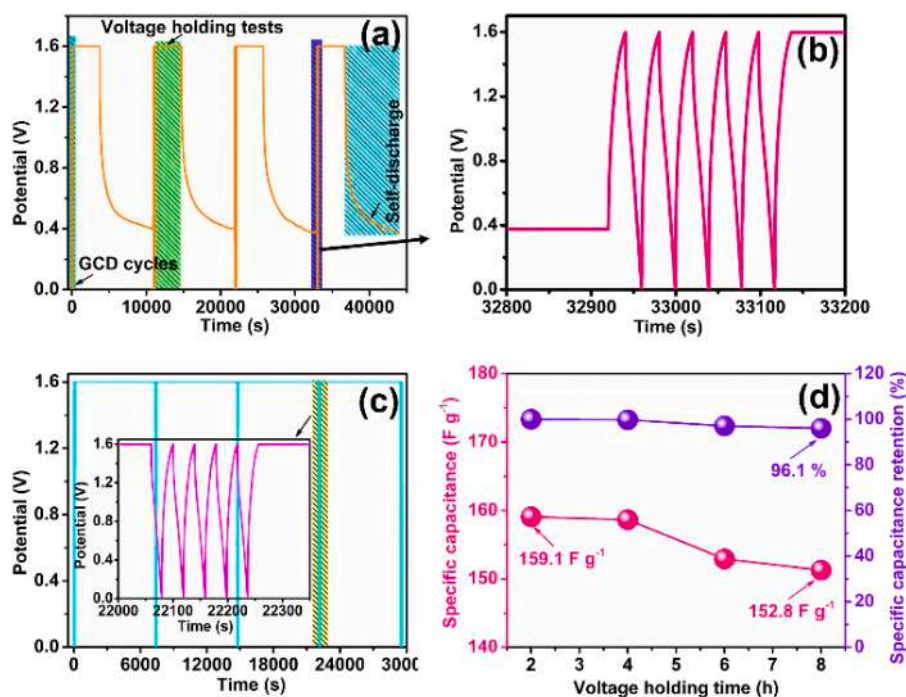
Fig. 5. (a) GCD cycles + 2 h VHT + 2 h SDT (16 h of electrochemical investigation), (b) after more than 12 h GCD cycles + VHT + SDT, the GCD cycles between SDT and VHT, (c) GCD cycles + 8 h VHT (inset- GCD cycles between VHT), and (d) the specific capacitance and stability (specific capacitance retention) of ZC-CSH SSC.
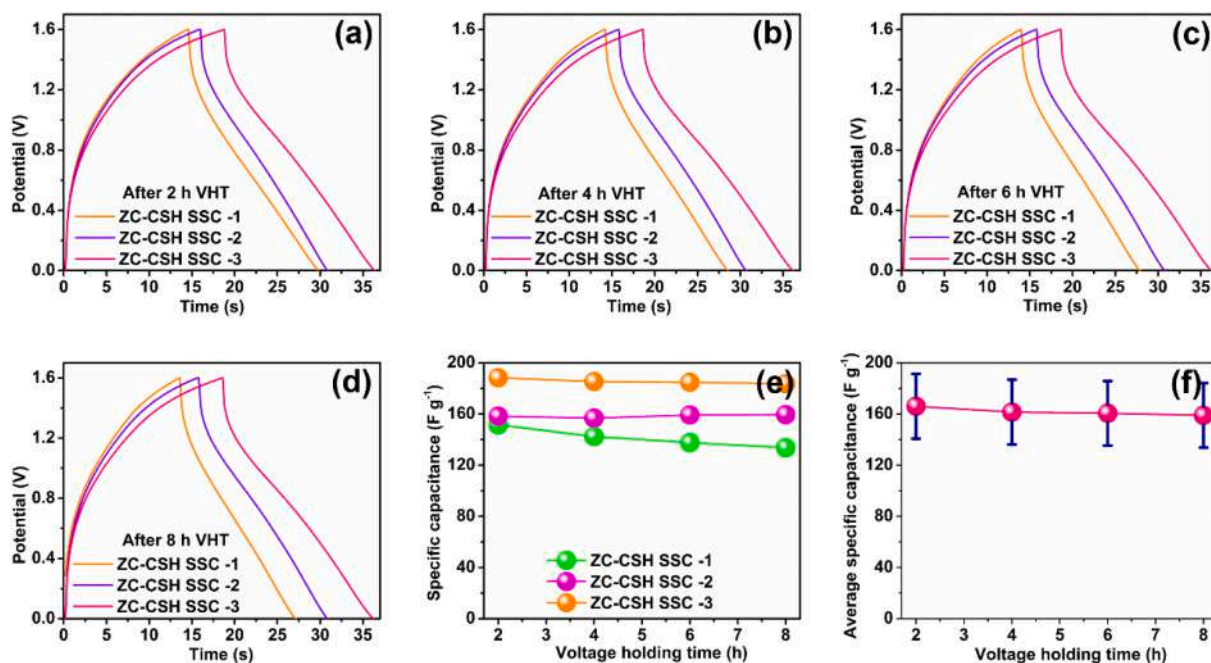

Fig. 6. (a-d) Reproducibility test of three ZC-CSH SSCs using GCD cycling after 2, 4, 6, and 8 h of VHT, (e) specific capacitance evaluated from the discharge area of GCD plots after different voltage holding tests, and (f) average specific capacitance of three ZC-CSH SSCs with an error bar.

capacitances of the ZC-CSH SSC-1 and ZC-CSH SSC-3 were found to be decreased from 151.6 and 188.4F g^{-1} to 133.6 and 183.7F g^{-1}, respectively, after 8 h of VHT. However, the specific capacitance of ZC-CSH SSC-2 is increased from 158.3 to 159.5F g^{-1} after 8 h of the VHT. Fig. 6(f) indicates the slight reduction in the average specific capacitance of all three similar devices from 166.1F g^{-1} to 158.9F g^{-1} after 8 h of VHT. It shows the excellent reproducibility of the ZC-CSH SSC. However, more study needs to be carried out for the reproducibility of the supercapacitors based on different nanostructures.

Moreover, the Leakage current (LC) of the ZC-CSH SSC plays a vital role in supercapacitor applications. In this study, the LC was recorded during the 2, 4, 6, and 8 h VHT, respectively, after the ZC-CSH SSC was charged up to the voltage of 1.6 V. Fig. 7(a) shows the LC (inset illustrates the enlarged portion of LC) of the ZC-CSH SSC. The LC of the ZC-CSH SSC increased with raising the voltage holding time. Initially, the LC was found to 0.15, 0.21, 0.26, and 0.28 mA after a couple of seconds; further, it reduces to 0.07, 0.11, 0.15, and 0.17 mA after 2, 4, 6, and 8 h of VHTs. Therefore, it is concluded that the ZC-CSH SSC exhibits a
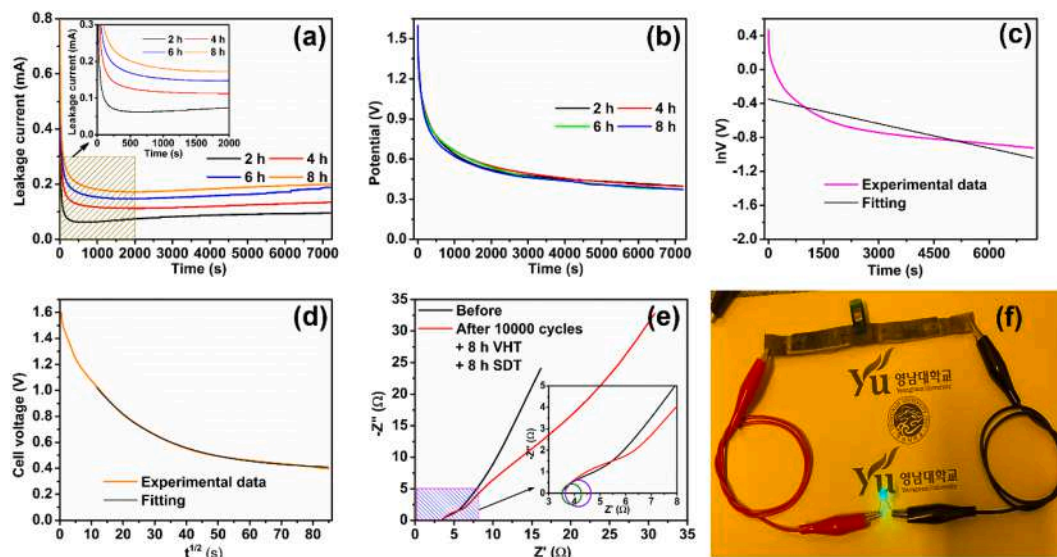
Fig. 7. (a) Leakage current, (b) four different cycles of self-discharge characteristics after 2, 4, 6, and 8 h voltage holding test, (c) ln V vs. t plot, (d) V vs. $t^{1/2}$ plot, (e) Nyquist plot and (f) illumination of a green LED using two ZC-CSH SSCs in series.

minimal LC, which results in excellent stability during the VHTs. The existence of LC in the ZC-CSH SSC during different VHTs may occur due to the following reasons; unwanted Faradaic reactions, ohmic leakage, functional groups with surface oxygen, charge redistribution, and impurities formation on the electrode surface [41,42]. The increase in LC from 2 to 8 h of voltage holding test may lead to enhanced chemical reactivity associated with water electrolysis [43].

Self-discharge (SD) is an inherent process where ions diffuse out of the Helmholtz layer to the extent of their equilibrium state of disorder, which results in the dissipation of supercapacitors' stored energy [44]. However, during the Self-discharge test (SDT) of supercapacitors, chemical reactions barely arise in the Helmholtz layer charge structure; therefore, the driving force for SD could be either a potential field or a concentration gradient [45,46]. The ZC-CSH SSC experiences the SD behavior in its charged state because of the thermodynamic driving force, which generates high free energy in the charge state compared with low free energy in the discharged state [47]. Fig. 7(b) shows the 2, 4, 6, and 8 h open-circuit decay of the ZC-CSH SSC's voltage after charging up to 1.6 V at 12.4 A g^{-1}. The initial voltage decreased exponentially with time, and after that, it became nearly constant. The ZC-CSH SSC represented the voltage drop from 1.6 V to 0.39, 0.38, 0.37, and 0.36 V over 2, 4, 6, and 8 h VHTs and SDT. These variations in the collective extent of charges/electrolyte ions result in a quick potential drop at the electric double layer of the ZC-CSH SSC at starting the SD process [48]. There are two kinds of Self-discharge (SD) mechanisms in supercapacitors: (i) potential driving SD and (ii) diffusion-controlled SD. The potential driving SD process by ohmic leakage in supercapacitors can be expressed as Eq. (2) [48];

$$V = V_i \exp\left(-\frac{t}{RC}\right) \tag{2}$$

where V is the voltage variation during SD, V_i is the primary voltage of the ZC-CSH SSC, m is the diffusion parameter, t is the SD time, and RC is a time constant of the self-discharge. Fig. 7(c) displays the ln V vs. t plot of the ZC-CSH SSC and fitting by applying Eq. (2). It was observed that the SD characteristic is not well fitted and deviated from the actual experimental characteristics. Therefore, it was concluded that the ZC-CSH SSC's SD characteristic is not due to the potential driving model.

The diffusion-controlled process in the ZC-CSH SSC can be written in Eq. (3) [48];

$$V = V_i - m t^{\frac{1}{2}} \tag{3}$$

where m is the diffusion factor which signifies the diffusion rate of

the electrolyte ions near the electrode surface. The diffusion-controlled process Eq. (3) was applied to the ZC-CSH SSC's SD experimental results [Fig. 7(d)]. Fig. 7(d) illustrates the V vs. $t^{1/2}$ plot and fitting by applying Eq. (3). Eq. (3) fitted tightly with the experimental results of SD. Consequently, it can be considered as a piece of evidence that the SD of the ZC-CSH SSC follows the diffusion-controlled Faradaic processes.

Electrochemical impedance spectroscopy (EIS) is a useful measurement of electrode material, electrolyte, charge transfer resistance, and diffusion coefficient. Fig. 7(e) shows the ZC-CSH SSC's EIS spectra before/ after 10,000 GCD cycles and 8 h VHT & 8 h SDT. The intercepts on the Z' axis at the high-frequency Exhibit equivalent series resistance (ESR). This ESR combines electrolyte resistance, electrode materials resistance, current collector, and contact resistance [49,50]. The ESR for the ZC-CSH SSC was 3.5 Ω and 3.7 Ω after 10,000 GCD cycles, 8 h VHT, and 8 h SDT. A slight swing in ESR value provides the evidence about the electrolyte resistance and grain boundary resistance, which is minimum before and after 8 h VHT and SDT. The semicircle's diameters show the ZC-CSH SSC charge transfer resistance at the electrolyte-electrode interface, as depicted in the inset. The charge transfer resistance was 0.8 Ω and 0.9 Ω before and after 10,000 GCD cycles, 8 h VHT, and 8 h SDT. This charge transfer resistance is dependent on electrode geometry, electrolyte solution resistivity or viscosity [51]. The linear portion at the low-frequency area is ascribed to the Warburg impedance (diffusion resistance) exhibited due to the controlled diffusion and transport of electrolyte ions through the ZC-CSH electrodes [52]. The Warburg impedance was 2.5 Ω and 7.5 Ω after 10,000 GCD cycles, 8 h VHT, and 8 h SDT. Fig. 7(f) demonstrates the illumination of a green LED using two ZC-CSH SSCs in series.

Table 1 shows a comparison between the ZnO-Co$_3$O$_4$ core–shell heterostructure based symmetric supercapacitor (ZC-CSH SSC) (present work) with the other results of reported ZnO-Co$_3$O$_4$ based symmetric and asymmetric supercapacitors. As discussed in Table 1, the ZC-CSH SSC shows high or comparable specific capacitance, energy density, stability using GCD cycles with the other reported results [18,21,24,53–56]. However, these studies did not study the stability using voltage holding tests, leakage current, and self-discharge, which is highly desirable for commercial supercapacitors. Consequently, it is concluded that the ZC-CSH SSC illustrates excellent electrochemical properties such as high specific capacitance, high energy density, excellent stability using 10,000 GCD cycles and 8 h VHTs + 8 h SDT, and minimal leakage current. Therefore it can be helpful in portable electronic gadgets for energy storage device applications.

Table 1

Comparing the present work with the reported ZnO-Co$_3$O$_4$ nanostructure-based symmetric and asymmetric supercapacitors.

| Electrode materials	Specific capacitance	Energy density	Stability GCD[1]	VHTs[2]	Leakage current	Self-discharge voltage	Ref.
ZnO-Co$_3$O$_4$ core-shell heterostructure	177.0F g^{-1} at 1.4 A g^{-1}	39.3 W h kg^{-1}	92.8 % after 10,000 cycles	96.1 % after 8 h	0.06 mA	0.36 V after 8 h	This work
ZnO-Co$_3$O$_4$ nanocomposite	165.0F g^{-1} at 2 mVs^{-1}	4.1 W h kg^{-1}	–	–	–	–	18
ZnO/Co$_3$O$_4$–450 //AC	153.0F g^{-1} at 1 A g^{-1}	47.7 W h kg^{-1}	–	–	–	–	21
ZnO/Co$_3$O$_4$ nanobundle arrays & graphene	198.0F g^{-1} at 1 A g^{-1}	70.4 W h kg^{-1}	86.5 % after 5000 cycles	–	–	–	24
rGO/HTZIF3// rGO	~95.0F g^{-1}at 5 mVs^{-1}	12.4 W h kg^{-1}	87.0 % after 2000 cycles	–	–	–	53
Co$_3$O$_4$@NiO/ZnO//AC	~290.0mF cm^{-2} at 2 mA cm^{-2}	162.0 µW h cm^{-2}	93.0 % after 10,000 cycles	–	–	–	54
ZnO/Co$_3$O$_4$/NiO-2 //AC	~274.0F g^{-1} at 1 A g^{-1}	95.8 Wh kg^{-1}	94.5 % after 10,000 cycles	–	–	–	55
Co$_3$O$_4$/ZnO//AC	~180.0F g^{-1} at 1 A g^{-1}	43.2 W h kg^{-1}	–	–	–	–	56

[1] GCD – Galvanostatic charging-discharging

[2] VHTs – Voltage holding tests.

3.2.3. Self-discharge mechanisms

Fig. 8 shows the schematic illustration of the ZC-CSH SSC's self-discharge mechanisms. Fig. 8(a) demonstrates the self-discharge mechanism due to the charge redistribution process. The outer surface of ZC-CSH electrodes in ZC-CSH SSC was charged more quickly than the inner surface. Therefore, when the outer surface-exposed region of the ZC-CSH electrodes in the ZC-CSH SSC achieved the required potential before the material's inner surface. The potential difference between ZC-CSH electrodes' inner and outer surfaces in the ZC-CSH SSC is a driving force leading to the transfer of charges in the inaccessible region to balance charge propagation called the charge redistribution [57,58]. In the ZC-CSH SSC, the potential was measured at the outer surface of the ZC-CSH electrodes. When the charges were transferred from the outer surface to the inner surface due to the charge redistribution process [59], the measured potential at the outer surface drops causes self-discharge. Further, in the ZC-CSH SSC's discharged state, the charges moved towards the outer surface from the inner surface for charge equilibrium due to charge redistribution causes self-discharge [60]. When the ZC-CSH SSC is charged, electrolyte ions are attracted to the oppositely charged electrode edges, creating various bonds in interca-lated capacitance. Fig. 8(b) illustrates the direct intercalation between Na$_2$SO$_4$ electrolyte ions and the ZC-CSH surface, or the non-existence of functional groups on the ZC-CSH electrode surface, which leads to a tight-bonding model; however, the ZC-CSH electrode surface having a functional group forms a loose-bonding model [61,45]. It is due to an increasing distance between the charges of electrolyte ions and the ZC-CSH electrode surface, which results in the weakening of the attractive force between electrolyte ions and the ZC-CSH electrode surface [61,48]. Therefore, it is concluded that the self-discharge mechanism may be due to the following reasons: (i) the existence of functional group on the electrode materials surface or loose bonding model, (ii) charge redistribution process at the ZC-CSH SSC's charged and discharged state, and (iii) fast interactions of the Na$_2$SO$_4$ electrolyte ions with the ZC-CSH electrode surface [61,62].

4. Conclusions

In conclusion, we studied the stability using the voltage holding tests and insights of the self-discharge mechanism of ZnO-Co$_3$O$_4$ core-shell heterostructures (ZC-CSH) SSC. As a result, the ZC-CSH SSC reveals a wide voltage window, high power density, specific capacitance, and energy density. More importantly, the ZC-CSH SSC unveils excellent stabilities of 92.8 % and 96.1 % by 10,000 GCD cycles and 8 h VHT, respectively. The ZC-CSH SSC discloses outstanding reproducibility, which was investigated using the three similar ZC-CSH SSCs. The ZC-CSH SSC illustrates a nominal leakage current during the VHT, further confirming the supercapacitor's operational reliability. The self-
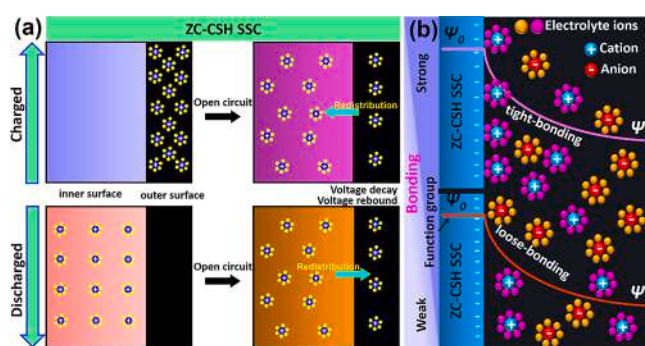
Fig. 8. (a) Self-discharge mechanisms of the ZC-CSH SSC due to charge redis-tribution, and (b) Self-discharge mechanisms of the ZC-CSH SSC due to tight-bonding (strong interactions) and loose-bonding (weak interactions) models.

discharge results indicate the charge redistribution by resistive path-ways. It is believed that the study of voltage holding tests and illustra-tion/ visualization of the self-discharge mechanisms can draw an insight to reduce the shortcomings (such as leakage current and voltage dissi-pation) of a practical supercapacitor for futuristic energy storage applications.

Declaration of Competing Interest

The authors declare that they have no known competing financial interests or personal relationships that could have appeared to influence the work reported in this paper.

Acknowledgments

Appendix A. Supplementary data

Supplementary data to this article can be found online at https://doi.org/10.1016/j.cej.2021.131895.

References

[1] C. Yu, J. An, R. Zhou, H. Xu, J. Zhou, Q. Chen, G. Sun, W. Huang, Microstructure design of carbonaceous fibers: a promising strategy toward high-performance weaveable/wearable supercapacitors, Small 16 (2020) 2000653.

[2] (a) Y. Wang, H. Jiang, R. Zheng, J. Pan, J. Niu, X. Zou, C. Jia, A flexible, electrochromic, rechargeable Zn-ion battery based on actiniae-like self-doped polyaniline cathode, J. Mater. Chem. A 8 (2020) 12799–12809;
(b) A. Sanger, A. Kumar, A. Kumar, P.K. Jain, Y.K. Mishra, R. Chandra, Silicon carbide nanocauliflowers for symmetric supercapacitor devices, Ind. Eng. Chem. Res. 55 (2016) 9452–9458.

[3] B. Shen, Y. Li, N. Sun, Y. Zhao, X. Hao, Enhanced energy-storage performance of an all-inorganic flexible bilayer-like antiferroelectric thin film via using electric field engineering, Nanoscale 12 (2020) 8958–8968;
(b) J.S. Shaikh, N.S. Shaikh, S. Sabale, N. Parveen, S.P. Patil, Y.K. Mishra, P. Kanjanaboos, S. Praserthdam, C.D. Lokhande, A phosphorus integrated strategy for supercapacitor: 2D black phosphorus-doped and phosphorus-doped material, Mater. Today Chem. 21 (2021), 100480.

[4] (a) C. Ogata, R. Kurogi, K. Hatakeyama, T. Taniguchi, M. Koinuma, Y. Matsumoto, All-graphene oxide device with tunable supercapacitor and battery behaviour by the working voltage, Chem. Commun. 52 (2016) 3919–3922;
(b) A. Kumar, A. Sanger, A. Kumar, Y.K. Mishra, R. Chandra, Performance of high energy density symmetric supercapacitor based on sputtered MnO_2 nanorods, ChemistrySelect 1 (2016) 3885–3891.

[5] (a) S. Ghosh, S. Barg, S.M. Jeong, K. Ken Ostrikov, Heteroatom-doped and oxygen-functionalized nanocarbons for high-performance supercapacitors, Adv. Energy Mater. 10 (2020) 2001239;
(b) P.K. Panda, A. Grigoriev, Y.K. Mishra, R. Ahuja, Progress in supercapacitors: roles of two dimensional nanotubular materials, Nanoscale Adv. 2 (2020) 70–108.

[6] Q. Zhang, J. Zhao, Y. Wu, J. Li, H. Jin, S. Zhao, L. Chai, Y. Wang, Y. Lei, S. Wang, Rapid and controllable synthesis of nanocrystallized nickel-cobalt boride electrode materials via a mircoimpinging stream reaction for high performance supercapacitors, Small 16 (2020) 2003342.

[7] (a) S. Kandambeth, J. Jia, H. Wu, V.S. Kale, P.T. Parvatkar, J.C. Jóźwiak, S. Zhou, X. Xu, Z.O. Ameur, E.A. Hamad, A.-H. Emwas, O. Shekhah, H.N. Alshareef, M. Eddaoudi, Covalent organic frameworks as negative electrodes for high-performance asymmetric supercapacitors, Adv. Energy Mater. 10 (2019) 2001673;
(b) R. Yuksel, O. Buyukcakir, P.K. Panda, S.H. Lee, Y. Jiang, D. Singh, S. Hansen, R. Adelung, Y.K. Mishra, R. Ahuja, R.S. Ruoff, Necklace-like nitrogen-doped tubular carbon 3D frameworks for electrochemical energy storage, Adv. Funct. Mater. 30 (2020) 1909725.

[8] M. Huang, F. Li, F. Dong, Y.X. Zhang, L.L. Zhang, MnO_2-based nanostructures for high-performance supercapacitors, J. Mater. Chem. A 3 (2015) 21380–21423.

[9] F. Wang, X. Wu, X. Yuan, Z. Liu, Y. Zhang, L. Fu, Y. Zhu, Q. Zhou, Y. Wu, W. Huang, Latest advances in supercapacitors: from new electrode materials to novel device designs, Chem. Soc. Rev. 46 (2017) 6816–6854.

[10] J. Xu, Z. Chen, J.A. Zapien, C.-S. Lee, W. Zhang, Surface engineering of ZnO nanostructures for semiconductor-sensitized solar cells, Adv. Mater. 26 (2014) 5337–5367.

[11] Y. Jia, Z. Wang, X.-Q. Qiao, L. Huang, S. Gan, D. Hou, J. Zhao, C. Sun, D.-S. Li, A synergistic effect between S-scheme heterojunction and noble-metal free cocatalyst to promote the hydrogen evolution of $ZnO/CdS/MoS_2$ photocatalyst, Chem. Eng. J. 424 (2021), 130368.

[12] Y.K. Mishra, R. Adelung, ZnO tetrapod materials for functional applications, Mater. Today 21 (2018) 631–651.

[13] N. Luo, Y. Chen, D. Zhang, M. Guo, Z. Xue, X. Wang, Z. Cheng, J. Xu, High-sensitive mems hydrogen sulfide sensor made from PdRh bimetal hollow nanoframe decorated metal oxides and sensitization mechanism study, ACS Appl. Mater. Interfaces 12 (2020) 56203–56215.

[14] C.-L. Hsu, Y.-J. Fang, T.-J. Hsueh, S.-H. Wang, S.-J. Chang, Nonenzymatic glucose sensor based on Au/ZnO core–shell nanostructures decorated with au nanoparticles and enhanced with blue and green light, J. Phys. Chem. B 121 (2017) 2931–2941.

[15] D. Kim, K.Y. Woo, J.H. Han, T.-W. Lee, H.S. Lee, Y.-H. Cho, K.C. Choi, Nanosinusoidal surface zinc oxide for optical out-coupling of inverted organic light-emitting diodes, ACS Photonics 5 (2018) 4061–4067.

[16] D. Dworschak, C. Brunnhofer, M. Valtiner, Photocorrosion of ZnO single crystals during electrochemical water splitting, ACS Appl. Mater. Interfaces 12 (2020) 51530–51536.

[17] T.A. Geleta, T. Imae, Nanocomposite photoanodes consisting of p-NiO/n-ZnO heterojunction and carbon quantum dot additive for dye-sensitized solar cells, ACS Appl. Nano Mater. 4 (2021) 236–249.

[18] I. Shaheen, K.S. Ahmad, C. Zequine, R.K. Gupta, A.G. Thomas, M.A. Malik, Green synthesis of $ZnO–Co_3O_4$ nanocomposite using facile foliar fuel and investigation of its electrochemical behaviour for supercapacitors, New J. Chem. 44 (2020) 18281–18292.

[19] S. Adhikari, S. Selvaraj, S.-H. Ji, D.-H. Kim, Encapsulation of Co_3O_4 nanocone arrays via ultrathin NiO for superior performance asymmetric supercapacitors, Small 16 (2020) 2005414.

[20] I. Rabani, J. Yoo, H.-S. Kim, D.V. Lam, S. Hussain, K. Karuppasamy, Y.-S. Seo, Highly dispersive Co_3O_4 nanoparticles incorporated into a cellulose nanofiber for a high-performance flexible supercapacitor, Nanoscale 13 (2021) 355–370.

[21] M. Gao, W.-K. Wang, Q. Rong, J. Jiang, Y.-J. Zhang, H.-Q. Yu, Porous ZnO-coated Co_3O_4 nanorod as a high-energy-density supercapacitor material, ACS Appl. Mater. Interfaces 10 (2018) 23163–23173.

[22] D. Cai, H. Huang, D. Wang, B. Liu, L. Wang, Y. Liu, Q. Li, T. Wang, High-performance supercapacitor electrode based on the unique $ZnO@Co_3O_4$ core/shell heterostructures on nickel foam, ACS Appl. Mater. Interfaces 6 (2014) 15905–15912.

[23] H. Zhu, J. Liu, Q. Zhang, J. Wei, High electrochemical performance of metal azolate framework-derived ZnO/Co_3O_4 for supercapacitors, Int. J. Energy Res. 44 (2020) 8654–8665.

[24] N. Hu, W.H. Gong, L. Huang, P.K. Shen, Ultrahigh energy density asymmetric electrochemical capacitors based on flower-like ZnO/Co_3O_4 nanobundle arrays and stereotaxically constricted graphene, J. Mater. Chem. A 7 (2019) 1273–1280.

[25] J. Balamurugan, T.T. Nguyen, D.H. Kim, N.H. Kim, J.H. Lee, 3D nickel molybdenum oxyselenide ($Ni_{1-x}Mo_xOSe$) nano architectures as advanced multifunctional catalyst for Zn-air batteries and water splitting, Appl. Catal. B 286 (2021), 119909.

[26] R. Vishnuraj, K.K. Karuppanan, M. Aleema, B. Pullithadathil, Boosting the performance of NO_2 gas sensors based on n–n type mesoporous $ZnO@In_2O_3$ heterojunction nanowires: in situ conducting probe atomic force microscopic elucidation of room temperature local electron transport, Nanoscale Adv. 2 (2020) 4785–4797.

[27] K. Xiang, Z. Song, D. Wu, X. Deng, X. Wang, W. You, Z. Peng, L. Wang, J.-L. Luo, X.-Z. Fu, Bifunctional $Pt–Co_3O_4$ electrocatalysts for simultaneous generation of hydrogen and formate via energy-saving alkaline seawater/methanol co-electrolysis, J. Mater. Chem. A 9 (2021) 6316–6324.

[28] L. Li, T. Tian, J. Jiang, L. Ai, Hierarchically porous Co_3O_4 architectures with honeycomb-like structures for efficient oxygen generation from electrochemical water splitting, J. Power Sources 294 (2015) 103–111.

[29] M. Guo, K. Xu, Y. Qu, F. Zeng, C. Yuan, Porous Co_3O_4/CoS_2 nanosheet-assembled hierarchical microspheres as superior electrocatalyst towards oxygen evolution reaction, Electrochim. Acta 268 (2018) 10–19.

[30] Y. Sun, Y. Wang, L. Liu, B. Liu, Q. Zhang, D. Wu, H. Zhang, X. Yan, Towards the understanding of acetonitrile suppressing salt precipitation mechanism in a water-in-salt electrolyte for low-temperature supercapacitors, J. Mater. Chem. A 8 (2020) 17998–18006.

[31] H.A. Andreas, B.E. Conway, Examination of the double-layer capacitance of an high specific-area C-cloth electrode as titrated from acidic to alkaline pHs, Electrochim. Acta 51 (2006) 6510–6520.

[32] R. Wang, X. Yan, J. Lang, Z. Zheng, P. Zhang, A hybrid supercapacitor based on flower-like $Co(OH)_2$ and urchin-like VN electrode materials, J. Mater. Chem. A 2 (2014) 12724–12732.

[33] M. Ma, Z. Shi, Y. Li, Y. Yang, Y. Zhang, Y. Wu, H. Zhao, E. Xie, High-performance 3 V "water in salt" aqueous asymmetric supercapacitors based on VN nanowire electrodes, J. Mater. Chem. A 8 (2020) 4827–4835.

[34] T. Brezesinski, J. Wang, S.H. Tolbert, B. Dunn, Ordered mesoporous $\alpha-MoO_3$ with iso-oriented nanocrystalline walls for thin-film pseudocapacitors, Nat. Mater. 9 (2010) 146–151.

[35] C. Niu, C. Han, H. Song, S. Yuan, W. Hou, Intercalation pseudocapacitance behavior of few-layered molybdenum sulfide in various electrolytes, J. Colloid Interface Sci. 561 (2020) 117–126.

[36] G. Zhang, T. Guan, N. Wang, J. Wu, J. Wang, J. Qiao, K. Li, Small mesopore engineering of pitch-based porous carbons toward enhanced supercapacitor performance, Chem. Eng. J. 399 (2020), 125818.

[37] Z. Li, Y. Dall`Agnese, J. Guo, H. Huang, X. Liang, S. Xu, Flexible freestanding all-MXene hybrid films with enhanced capacitive performance for powering a flex sensor, J. Mater. Chem. A 8 (2020) 16649–16660.

[38] Q. Li, Z. Dai, J. Wu, W. Liu, T. Di, R. Jiang, X. Zheng, W. Wang, X. Ji, P. Li, Z. Xu, X. Qu, Z. Xu, J. Zhou, Fabrication of ordered macro-microporous single-crystalline MOF and its derivative carbon material for supercapacitor, Adv. Energy Mater. 10 (2020) 1903750.

[39] Y. Li, P. Kamdem, C. Cheng, X.-J. Jin, X. Liu, Hydrophilic "bridge" $H-C_3N_4$ stabilizing CuO onto graphenes with enhanced energy density for asymmetric supercapacitors, Sustain. Energy Fuels 4 (2020) 4196–4206.

[40] L. Xie, F. Su, L. Xie, X. Guo, Z. Wang, Q. Kong, G. Sun, A. Ahmad, X. Li, Z. Yi, C. Chen, Effect of pore structure and doping species on charge storage mechanisms in porous carbon-based supercapacitors, Mater. Chem. Front. 4 (2020) 2610–2634.

[41] A. Noori, M.F.E. Kady, M.S. Rahmanifar, R.B. Kaner, M.F. Mousavi, Towards establishing standard performance metrics for batteries, supercapacitors and beyond, Chem. Soc. Rev. 48 (2019) 1272–1341.

[42] R.K. Mishra, G. Jin Choi, Y. Sohn, S.H. Lee, J.S. Gwag, A novel RGO/N-RGO supercapacitor architecture for a wide voltage window, high energy density and long-life via voltage holding tests, Chem. Commun. 56 (2020) 2893–2896.

[43] M. Haque, Q. Li, A.D. Smith, V. Kuzmenko, P. Rudquist, P. Lundgren, P. Enoksson, Self-discharge and leakage current mitigation of neutral aqueous-based supercapacitor by means of liquid crystal additive, J. Power Sources 453 (2020), 227897.

[44] I.S. Ike, I. Sigalas, S. Iyuke, Understanding performance limitation and suppression of leakage current or self-discharge in electrochemical capacitors: a review, PCCP 18 (2016) 661–680.

[45] Q. Zhang, J. Rong, D. Ma, B. Wei, The governing self-discharge processes in activated carbon fabric-based supercapacitors with different organic electrolytes, Energy Environ. Sci. 4 (2011) 2152–2159.

[46] B.W. Ricketts, C. That, Self-discharge of carbon-based supercapacitors with organic electrolytes, J. Power Sources 89 (2000) 64–69.

[47] B.E. Conway, Electrochemical Supercapacitors: Scientific Fundamentals and Technological Applications, Kluwer Academic/Plenum, New York, London, 1999.

[48] Z. Wang, X. Chu, Z. Xu, H. Su, C. Yan, F. Liu, B. Gu, H. Huang, D. Xiong, H. Zhang, W. Deng, H. Zhang, W. Yang, Extremely low self-discharge solid-state

supercapacitors via the confinement effect of ion transfer, J. Mater. Chem. A 7 (2019) 8633–8640.

[49] A. Allison, H.A. Andreas, Minimizing the Nyquist-plot semi-circle of pseudocapacitive manganese oxides through modification of the oxide-substrate interface resistance, J. Power Sources 426 (2019) 93–96.

[50] T.G. Lim, B.T. Ho, J.W. Suk, High-performance and thermostable wire supercapacitors using mesoporous activated graphene deposited on continuous multilayer graphene, J. Mater. Chem. A 9 (2021) 4800–4809.

[51] C. Hitz, A. Lasia, Experimental study and modeling of impedance of the her on porous Ni electrodes, J. Electroanal. Chem. 500 (2001) 213–222.

[52] N. Yadav, S.A. Hashmi, Energy enhancement of quasi-solid-state supercapacitors based on a non-aqueous gel polymer electrolyte via a synergistic effect of dual redox additives diphenylamine and potassium iodide, J. Mater. Chem. A 8 (2020) 18266–18279.

[53] S. Borhani, M. Moradi, M.A. Kiani, S. Hajati, J. Toth, Co_xZn_{1-x} ZIF-derived binary Co_3O_4/ZnO wrapped by 3D reduced graphene oxide for asymmetric supercapacitor: Comparison of pure and heat-treated bimetallic MOF, Ceram. Int. 43 (2017) 14413–14425.

[54] H. Chen, J. Zhou, Q. Li, K. Tao, X. Yu, S. Zhao, Y. Hu, W. Zhao, L. Han, Core-shell assembly of Co_3O_4@NiO-ZnO nanoarrays as battery-type electrodes for high-performance supercapatteries, Inorg. Chem. Front. 6 (2019) 2481–2487.

[55] L. Zhu, C. Hao, S. Zhou, X. Wang, T. Zhou, Y. Guo, Ternary ZnO/Co_3O_4/NiO inherited layered core-shell structure from a double template for high performanced supercapacitor, J. Materiomics 7 (2021) 708–720.

[56] J. Xu, S. Liu, Y. Liu, Co_3O_4/ZnO nanoheterostructure derived from core-shell ZIF-8@ZIF-67 for supercapacitors, RSC Adv. 6 (2016) 52137–52142.

[57] H.A. Andreas, Self-discharge in electrochemical capacitors: a perspective article, J. Electrochem. Soc. 162 (2015) A5047–A5053.

[58] W.G. Pell, B.E. Conway, W.A. Adams, J. de Oliveira, Electrochemical efficiency in multiple discharge/recharge cycling of supercapacitors in hybrid EV applications, J. Power Sources 80 (1999) 134–141.

[59] M. Kaus, J. Kowal, D.U. Sauer, Modelling the effects of charge redistribution during self-discharge of supercapacitors, Electrochim. Acta 55 (2010) 7516–7523.

[60] J. Black, H.A. Andreas, Effects of charge redistribution on self-discharge of electrochemical capacitors, Electrochim. Acta 54 (2009) 3568–3574.

[61] Z. Wang, Z. Xu, H. Huang, X. Chu, Y. Xie, D. Xiong, C. Yan, H. Zhao, H. Zhang, W. Yang, Unraveling and regulating self-discharge behavior of $Ti_3C_2T_x$ MXene-based supercapacitors, ACS Nano 14 (2020) 4916–4924.

[62] Q. Zhang, J. Rong, B. Wei, A divided potential driving self-discharge process for single-walled carbon nanotube based supercapacitors, RSC Adv. 1 (2011) 989–994.